ACS OMEGA

Open Access

http://pubs.acs.org/journal/acsodf

Article

The Three-Dimensional Hierarchical Structure of Bi_x-$Sn_{1-x}O_2$ Used for Ultrasensitive Detection of Butanone under UV Irradiation

Wenjie Bi, Hu Chen, Shiwei Yang, Xiaohong Wang, Aoying Liu, Xinyue Ma, Haijiao Xie, and Shantang Liu*

Cite This: *ACS Omega* 2024, 9, 27932−27944

Read Online

ACCESS | Metrics & More | Article Recommendations

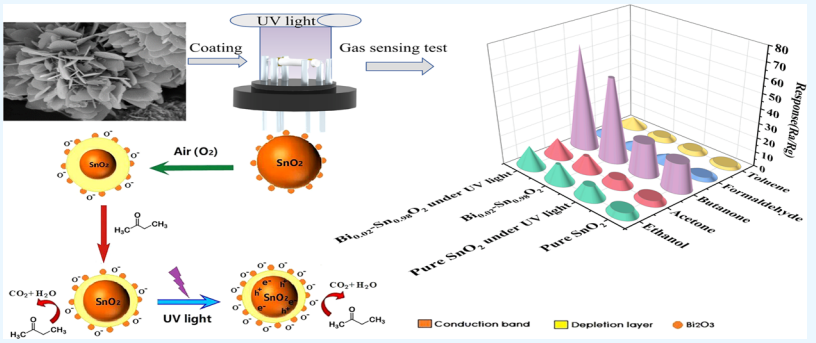

ABSTRACT: Recent studies have identified butanone as a promising biomarker in the breath of lung cancer patients, yet the understanding of its gas-sensing properties remains limited. A key challenge has been to enhance the gas-sensing performance of materials toward butanone, particularly under ultraviolet light exposure. Herein, we report the synthesis of a novel three-dimensional composite material composed of SnO_2 incorporated with Bi_2O_3 using facile hydrothermal and impregnation precipitation methods. Detailed physical and chemical characterizations were performed to assess the properties of the developed material. Upon activation with ultraviolet light, our composite exhibited exceptionally high sensitivity to butanone. Remarkably, the butanone response was nearly 3 times greater for the Bi_2O_3-loaded SnO_2 composite than for pristine SnO_2, achieving a response value of 70. This substantial improvement is due to the synergistic effect of the material's distinctive three-dimensional architecture and the presence of Bi_2O_3, which significantly augmented the gas-sensing capability of butanone. To elucidate the underlying gas-sensing mechanism, we conducted first-principles calculations using density functional theory (DFT). The computational analysis revealed that the Bi_2O_3-containing system possesses superior adsorption energy for butanone. Ultimately, our findings suggest that the Bi-SnO_2 composite holds great promise as an optimal sensing material for the detection of butanone under ultraviolet illumination.

INTRODUCTION

Human beings are increasingly exposed to toxic, harmful, flammable, and explosive gases from industrial production activities. These polluted gases have incredibly harmful impacts on the ecological environment and human health. To protect people from gas leakage and pollution, monitoring of flammable, explosive, toxic, and harmful gases are of great necessity.[1−4] The volatile organic compound (VOC) butanone is widely used in interior decoration, industrial production, and pharmaceutical manufacturing. It has been reported in the literature that butanone stimulates human eyes and neuron systems and is used as a biomarker in the exhaled breath of lung cancer patients.[5−9] Therefore, a material exhibiting efficient sensing of butanone gas is increasingly needed.

As vital gas-sensing materials, metal oxide semiconductors (MOSs) have been widely investigated due to their high sensitivities and low detection limits.[2,10,11] A number of gas-sensitive materials based on metal oxides have been synthesized and used to detect butanone. Vioto et al.[7] prepared a SiO_2@CoO core−shell structure with a high specific surface area, and gas-sensing test results showed that it detected 2-butanone effectively. The excellent gas-sensing performance may be attributed to the high surface area provided by the unique core−shell structure. Weng et al.[8] fabricated coral-like Zn-doped SnO_2 hierarchical structures assembled from nanorods. Its efficient detection of butanone may be attributed to the Zn doping and unique structure. As a

Received: December 15, 2023
Revised: May 21, 2024
Accepted: June 11, 2024
Published: June 18, 2024

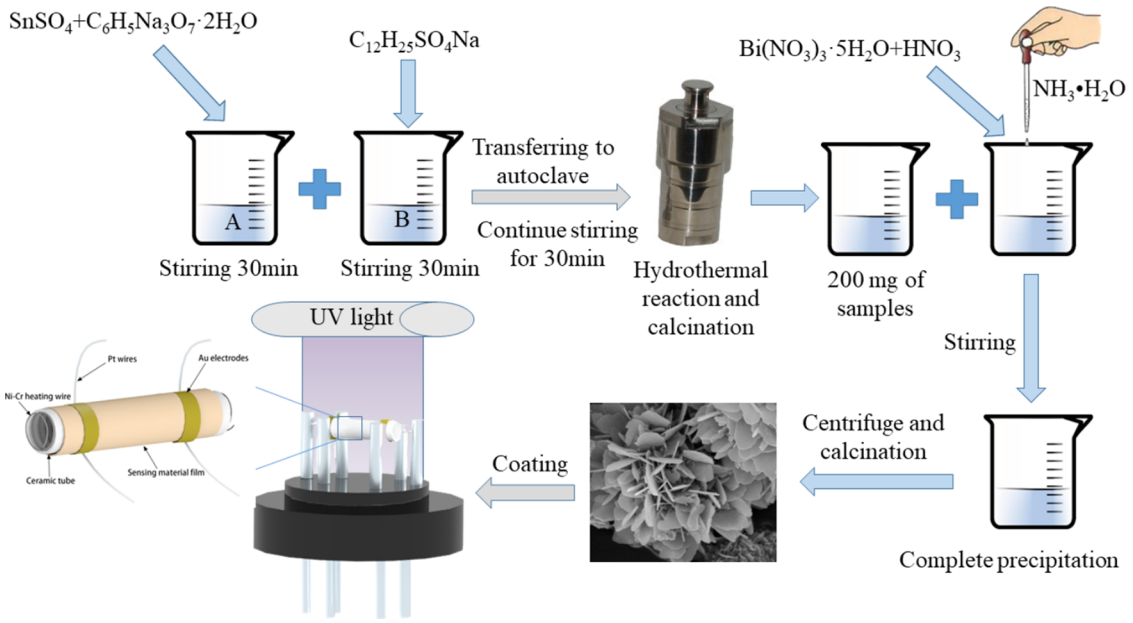

Figure 1. Schematic illustration of the synthesis of the Bi_x-$Sn_{1-x}O_2$ hierarchical structure.

typical MOS, SnO_2 is a wide band gap n-type semiconductor with high electron mobility. Sensors based on SnO_2 generally show excellent responses to various gases and have the advantages of low costs and long service lives. However, pure SnO_2-based sensors usually exhibit weak responses and poor selectivities and require high operating temperatures.[12−15]

According to literature reports, the gas-sensing properties of MOS materials are related to their unique physical and chemical properties and the microstructures of the surfaces.[16] Generally, materials with large specific surface areas and porous structures exhibit better gas-sensing performance.[15,17] The hierarchical structure constitutes a three-dimensional nanomaterial structure with a geometric shape formed by self-assembling of low-dimensional nanomaterials. Compared with other nanostructures, the three-dimensional hierarchical structure with the high specific surface area enables significantly enhanced gas detection by the material, which has excellent potential application value and research value.[18,19] Zhu et al.[20] prepared Y-doped SnO_2 hierarchical flower-like nanostructures via a one-step hydrothermal method. Characterization results indicated that the excellent sensitivity to formaldehyde was due to the Y-doping and the unique three-dimensional hierarchical structure. The sensitivities and selectivities of composite metal oxide-sensitive materials can be improved by changing the compositions. Therefore, this approach has received extensive attention from researchers.[21,22] Another effective method to enhance gas sensitivity is by combining other metal oxides with tin dioxide to form a composite structure. Such a structure not only increases the surface area for gas adsorption but also allows for the adjustment of the adsorption capacity, significantly enhancing the sensitivity of the sensor. Bang et al. grew Bi_2O_3 branches on SnO_2 nanotubes using the vapor−liquid−solid method, thereby developing a gas-sensitive material with excellent detection capabilities for NO_2 gas. The outstanding detection performance of this gas-sensitive material primarily stems from the high specific surface area generated by the Bi_2O_3 branches and the formed Bi_2O_3−SnO_2 heterostructure. As a typical n-type semiconductor, Bi_2O_3 is widely used in optoelectronic devices and gas sensors due to its excellent physical and chemical properties.[23,24] David et al.[23] successfully prepared a highly sensitive Ag/Bi_2O_3 composite nanomaterial using the precipitation method and applied it to monitor toluene in the air. The addition of Ag enhanced the gas-sensing properties of Bi_2O_3 through various mechanisms, thus achieving high-sensitivity detection of toluene gas at room temperature, making it a superior gas sensor material. In addition to compounding with other materials, the ability of the material to detect VOCs can also be improved by irradiation with ultraviolet (UV) light.[25−27] Hyodo et al.[28] reported that the gas-sensing performance of the material was improved by UV irradiation. Saidi et al.[29] reported that the capabilities of WO_3-based gas sensors for VOCs were significantly improved by UV irradiation. However, to the best of our knowledge, the use of Bi_2O_3-loaded SnO_2 nanostructures for detecting butanone with UV irradiation has yet to be studied. In conclusion, considering the important practical application value of developing a sensor that can effectively detect butanone, we note that current research on using the impregnation precipitation method to load Bi_2O_3 onto the surface of SnO_2 nanostructures is not sufficient. The impact of these materials on the gas sensitivity of butanone, especially under ultraviolet light irradiation, has not been explored in depth. Therefore, the aim of this study is to fill this gap in the research field and provide new insights for the efficient detection of butanone.

In this study, we synthesized SnO_2 with a three-dimensional hierarchical structure with a facile hydrothermal method and subsequently prepared a series of samples with different Bi_2O_3 loadings. Their use in detecting butanone under UV irradiation was investigated. The results indicated that combining the Bi_2O_3 and UV light significantly improved the gas-sensing performance. In addition, we explored the mechanism for butanone detection by the Bi containing SnO_2 with first-principles theoretical studies.

https://doi.org/10.1021/acsomega.3c09632
ACS Omega 2024, 9, 27932−27944

EXPERIMENTAL SECTION

Materials and Reagents. All chemicals in the experiments were of analytical grade and used without further purification. Stannous sulfate ($SnSO_4$), trisodium citrate ($C_6H_5Na_3O_7 \cdot 2H_2O$), sodium lauryl sulfate ($C_{12}H_{25}SO_4Na$), bismuth nitrate ($Bi(NO_3)_3 \cdot 5H_2O$), ammonia solution ($NH_3 \cdot H_2O$), and ethanol (C_2H_5OH) were purchased from Sinopharm Chemical Reagent Co., Ltd. Deionized water was used throughout all of the experiments.

Synthesis of the Bi_x-$Sn_{1-x}O_2$ Hierarchical Structure. In a typical synthesis process, initially, 5 mmol of tin(II) sulfate ($SnSO_4$) and 5 mmol of sodium citrate tribasic dihydrate ($C_6H_5Na_3O_7 \cdot 2H_2O$) were dissolved in 40 mL of a mixed solution consisting of deionized water and anhydrous ethanol at a volume ratio of 1:1. Subsequently, 0.5 mmol of sodium dodecyl sulfate ($C_{12}H_{25}SO_4Na$) was dissolved in 20 mL of deionized water. Afterward, these two solutions were stirred separately for 30 min at room temperature using a magnetic stirrer. Then, the two solutions were combined and stirred for another 30 min. Once stirring was complete, the solution was transferred to a stainless-steel autoclave lined with polytetrafluoroethylene and heated at 180 °C for 24 h. After the reaction was finished, the autoclave was allowed to cool naturally to room temperature. The collected precipitate was then centrifuged and washed several times with anhydrous ethanol and deionized water (8000 rpm for 10 min). Afterward, the product obtained from centrifugation was dried in an oven at 80 °C for 12 h. Finally, the dried powder was transferred to a muffle furnace and annealed at 500 °C for 2 h.

Using the impregnation method, we prepared a series of $Bi_xSn_{1-x}O_2$ hierarchical structure materials with molar ratios x = [Bi]/([Bi] + [Sn]) of 0.0, 1.0, 2.0, and 3.0. First, 200 mg of the sample was weighed and dispersed in 60 mL of deionized water with stirring. In the process of preparing the bismuth nitrate solution, an appropriate amount of bismuth nitrate ($Bi(NO_3)_3 \cdot 5H_2O$) was dissolved in dilute nitric acid. Then, the dispersed SnO_2 sample was mixed with a bismuth nitrate solution. During stirring, ammonia−water was added dropwise to adjust the pH to 11, followed by continued stirring at room temperature until precipitation occurs completely. The obtained precipitate was centrifuged and washed using a mixture of anhydrous ethanol and deionized water, a process that was repeated three times (8000 rpm for 10 min). Subsequently, the centrifuged product was dried in an oven at 80 °C for 12 h. Finally, the dried powder was transferred to a muffle furnace and annealed at 500 °C for 2 h.

A schematic diagram showing the Bi_x-$Sn_{1-x}O_2$ synthetic process and loading strategy is shown in Figure 1.

Material Characterizations. The composition and structure of the material were characterized with X-ray powder diffraction (XRD) (Bruker D8 Advance, with Cu Kα radiation (λ = 0.15406 nm), 40 kV, and 40 mA). The microscopic morphologies and sizes of the particles were recorded with a field emission scanning electron microscope (FESEM, Gemini SEM 300, 10.0 kV) equipped with an EDS detector. Energy dispersive X-ray spectroscopy (EDS, XFlash610-H) was used to study the distributions of the elements. To obtain more detailed information on the morphologies and structures of the samples, they were observed with a transmission electron microscope and a high-resolution transmission electron microscope (HRTEM, JEM- 2100, 200.0 kV). The specific surface areas and pore size distributions of the samples were measured with the Brunauer−Emmett−Teller (BET, ASAP 2460, Micromeritics Instruments) method. XPS measurements were performed by X-ray photoelectron spectroscopy (XPS, Thermo Scientific, ESCALAB 250XI, $h\nu$ = 1486.6 eV). Charge correction was carried out with the standard C 1s peak at 284.80 eV. UV−vis measurements were carried out with a PerkinElmer Lambda 750 spectrophotometer.

Fabrication and Measurement of Gas Sensors. The gas-sensing capabilities of the samples were measured with a WS-30B gas-sensing analysis system (Weisheng Instruments Co., Zhengzhou, China), and the gas sensor fabrication and gas-sensing test methods were previously reported.[30] In a typical sensor fabrication procedure, the synthesized samples with varying loading ratios were pulverized into fine powders with an agate mortar. One of the resulting powders was mixed with an appropriate amount of ethanol to form a viscous slurry, which was ground for 1 h. A ceramic tube was coated with the ground slurry using a fine brush, ensuring uniform coverage. The coated tube was subsequently dried in an oven at 80 °C for 2 h. A heating coil comprising a Ni−Cr alloy was inserted into the ceramic tube and then welded to the sensing element base. Subsequently, the ceramic tube was also welded to the sensing element base. To improve the stability of the device, the gas sensor was aged at 200 °C for 120 h. The relative humidity in the test chamber was approximately 20% during the test.

To ensure the accuracy and reliability of the gas sensors, we performed a series of calibration procedures before the measurements. First, based on the technical parameters and experimental scheme of the test system, we appropriately set the number of test channels, acquisition speed, test voltage, and other parameters. Then, we turned on the equipment, allowing the sensing elements to reach the working temperature and maintain it for a predetermined time. Subsequently, without adding any test gases, we conducted a baseline test on the test system. Afterward, we injected the target gas at a known concentration (such as butanone) into the gas chamber and recorded the response value of the corresponding gas-sensitive element. At different concentrations, we plotted the response curve according to the sensor's response and verified the sensitivity and precision of the sensor by comparing the actual response of the sensor with the theoretical value. After the above steps, we are confident that the gas sensors have been fully calibrated before measurement, thus ensuring the accuracy and reliability of the measurement results.

In this study, we utilized a static gas distribution method to evaluate the gas sensitivities of the sensors. During the gas-sensing tests, the UV light was provided by UV lamp tubes emitting a wavelength of 365 nm. The response of the gas sensor was calculated as $S = R_a/R_g$, where R_a is the resistance of the sensor in air and R_g is the resistance of the sensor in the target gas. The response times (T_{res}) and recovery times (T_{rec}) of the gas sensors were defined as the time required for the resistance to reach 90% of its steady-state value after insertion into or removed from the target gas to be measured.

RESULTS AND DISCUSSION

Structure and Composition Analysis. XRD analyses were conducted on samples with varying loading ratios, and the results are depicted in Figure 2. All of the samples exhibited strong diffraction peaks, demonstrating their high crystallinities. Additionally, no diffraction peaks from impur-

https://doi.org/10.1021/acsomega.3c09632
ACS Omega 2024, 9, 27932−27944

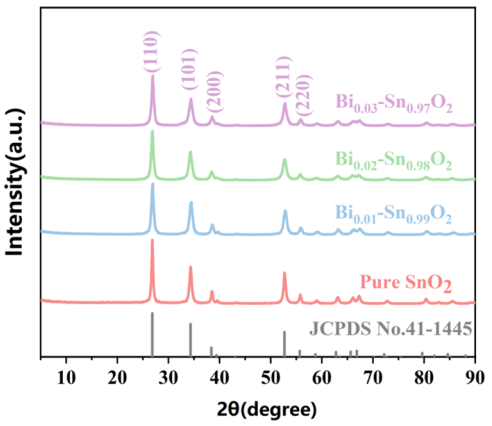

Figure 2. XRD patterns for Bi_x-$Sn_{1-x}O_2$ (x = 0.0, 1.0, 2.0, and 3.0%).

ities were detected. All of the diffraction peaks were indexed to the tetragonal rutile phase of SnO_2 (JCPDS No. 41-1445, space group $P4_2/mnm$, a = 4.738 Å, c = 3.187 Å).[11,15] No diffraction peaks for Bi or its oxides were found in the XRD spectrum. This was attributed to the low proportion of Bi on the SnO_2 surface, which surpass the XRD detection threshold.[15,31] The positions and half-height widths of the peaks were unchanged, suggesting that the crystalline SnO_2 was not affected by Bi_2O_3 loading.

The morphologies of the pure SnO_2 and $Bi_{0.02}$-$Sn_{0.98}O_2$ samples were characterized with field emission scanning electron microscopy (FESEM) (Figure 3). Figure 3a shows an FESEM image of the pure SnO_2 hierarchical structure. The image clearly displays the flower-like hierarchical structure, which was formed by self-assembly of nanosheets. Figure 3b shows higher magnification FESEM images, and the results indicated good homogeneity and a monodisperse morphology. The nanosheets present relatively smooth surfaces with edge thicknesses of approximately 20−30 nm. Figure 3c,d shows FESEM images of the $Bi_{0.02}$-$Sn_{0.98}O_2$ hierarchical structure at different magnifications. There were no significant changes in the structures and particle sizes of the samples after Bi loading, suggesting that the prepared SnO_2 samples were very stable. Figure 3d shows that a small number of nanoparticles were dispersed on the surfaces of the material. These particles could be precipitated by Bi_2O_3.

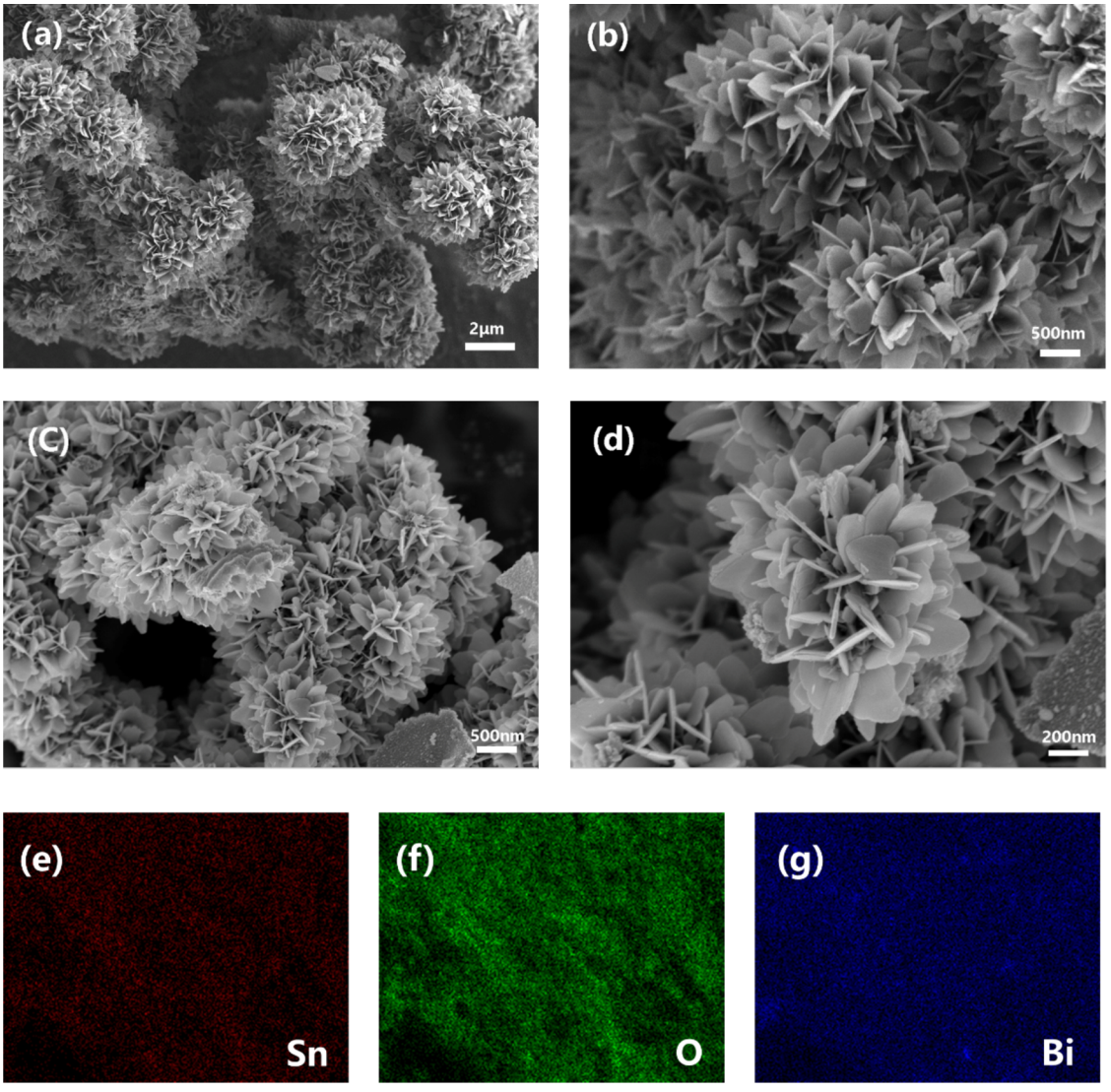

Figure 3. FESEM analyses with different loading ratios; (a, b) pure SnO_2, (c, d) $Bi_{0.02}$-$Sn_{0.98}O_2$, and (e−g) EDS element maps of $Bi_{0.02}$-$Sn_{0.98}O_2$.

https://doi.org/10.1021/acsomega.3c09632
ACS Omega 2024, 9, 27932−27944

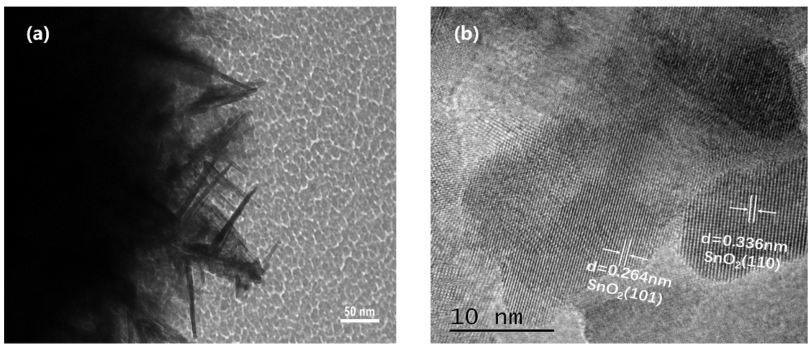

Figure 4. (a, b) TEM and HRTEM analyses of $Bi_{0.02}$-$Sn_{0.98}O_2$.

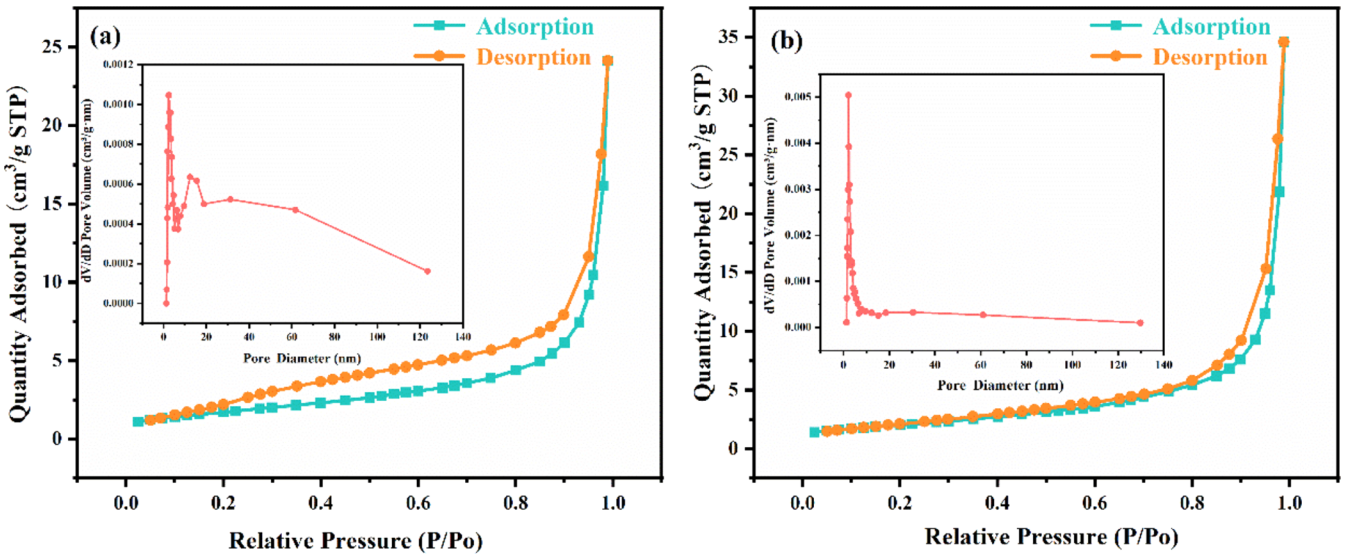

Figure 5. Typical N_2 absorption−desorption isotherms and Barrett−Joyner−Halenda (BJH) pore size distribution curves (inset) for pure SnO_2 (a) and $Bi_{0.02}$-$Sn_{0.98}O_2$ (b).

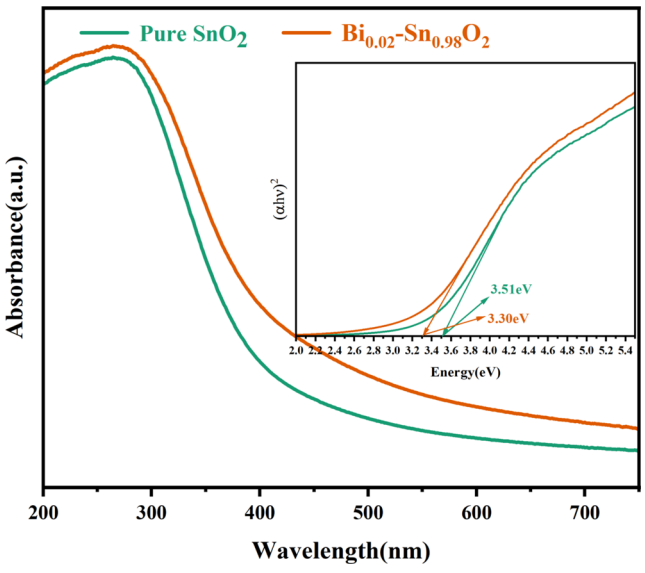

Figure 6. UV−vis absorption spectra and calculated band gaps (inset) for pure SnO_2 and $Bi_{0.02}$-$Sn_{0.98}O_2$.

To demonstrate the presence of Bi_2O_3 nanoparticles on the surface of the SnO_2, EDS elemental mapping was carried out with the 2.0 mol % Bi-SnO_2 nanostructure, as shown in Figure 3e−g, and this indicated the spatial distributions of Sn, O, and Bi, respectively. It is clear that Bi was uniformly distributed on the surface of the material.

The microstructure of the $Bi_{0.02}$-$Sn_{0.98}O_2$ was also characterized by TEM and HRTEM, and the results are shown in Figure 4. Figure 4a is a low-resolution TEM image, and it showed that the sample had a flower-like hierarchical structure assembled from nanosheets. The thicknesses of the nanosheets were approximately 20−30 nm, which was consistent with the results of the FESEM analysis. The HRTEM image (Figure 4b) revealed clear lattice fringes, indicating that the prepared samples were highly crystalline, which was consistent with the XRD analyses. The measured interplanar distances were approximately 0.336 and 0.264 nm, which corresponded to the (110) and (101) crystal planes of the tetragonal rutile phase of SnO_2, respectively.[32,33]

The BET-specific surface areas of the prepared samples were also determined. Figure 5a,b illustrates the nitrogen adsorption and desorption isotherms for pure SnO_2 and $Bi_{0.02}$-$Sn_{0.98}O_2$, respectively. The specific surface areas of the samples were determined with the Brunauer−Emmett−Teller (BET) equation, and the specific surface areas of the pure SnO_2 and $Bi_{0.02}$-$Sn_{0.98}O_2$ were 6.298 and 7.296 m^2/g, respectively. According to the IUPAC classification, the samples exhibited typical type IV adsorption isotherms with H3 hysteresis loops, indicating typical mesoporous structures.[34,35] The inset figure in Figure 5

https://doi.org/10.1021/acsomega.3c09632
ACS Omega 2024, 9, 27932−27944

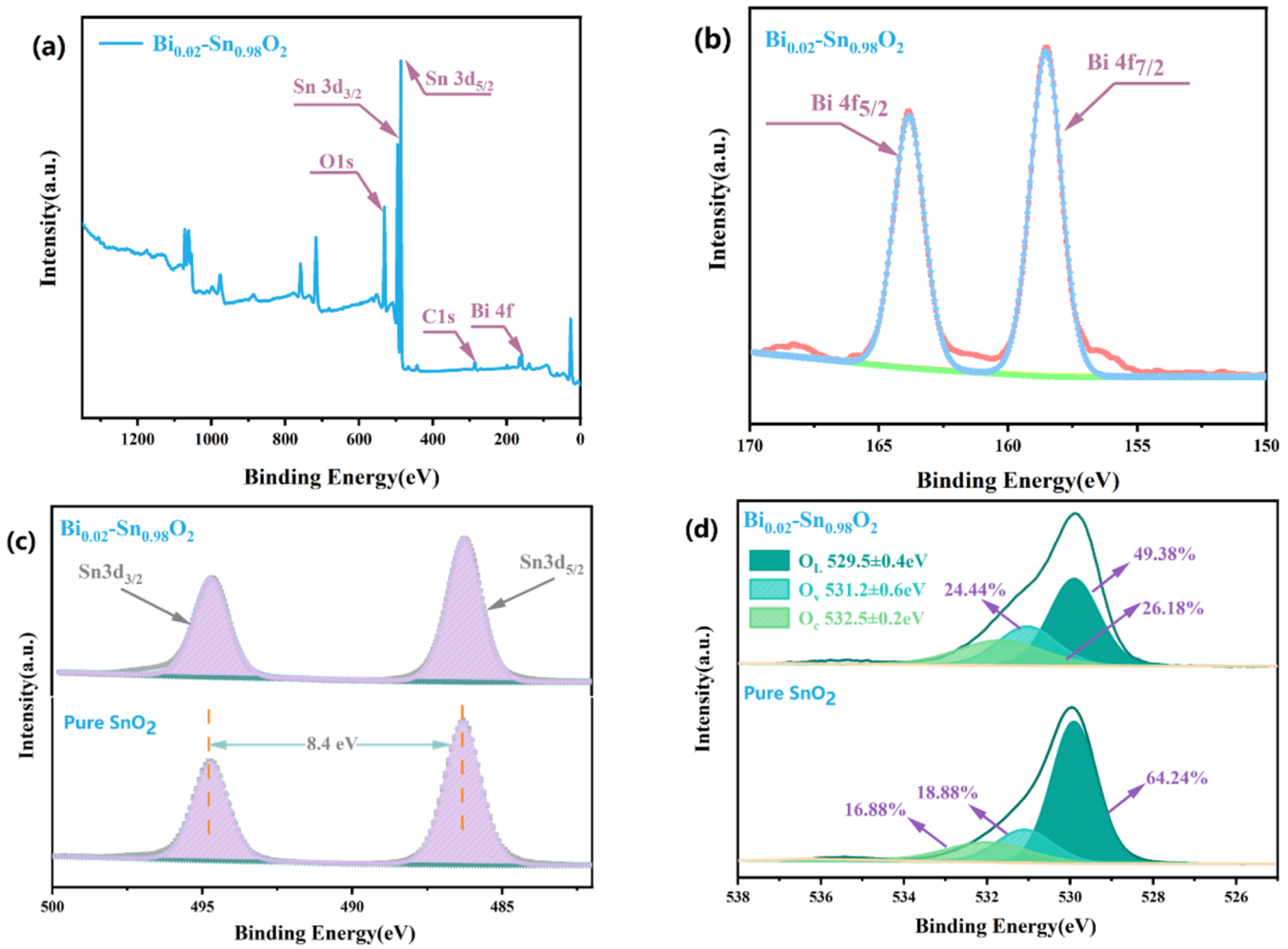

Figure 7. XPS data for pure SnO_2 and $Bi_{0.02}$-$Sn_{0.98}O_2$; (a) full spectrum and (b) Bi 4f, (c) Sn 3d, and (d) O 1s spectra.

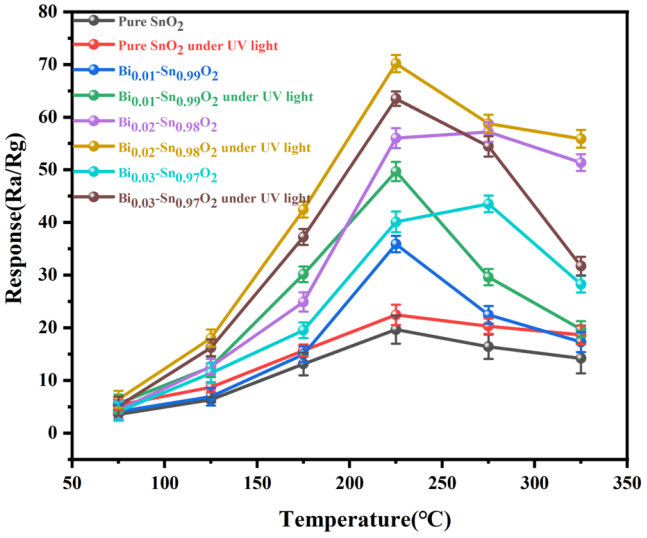

Figure 8. Responses of the samples with different loading ratios to 100 ppm butanone with or without UV irradiation.

illustrates the pore size distribution. The pore sizes of pure SnO_2 and $Bi_{0.02}$-$Sn_{0.98}O_2$ were concentrated within the range of 2−10 nm. The pore size distribution curves indicated relatively narrow pore size distributions, with median pore sizes of approximately 2.18 and 2.38 nm, respectively. The relatively narrow pore size distributions and large pore volumes of the material indicated high porosity, which is commonly associated with effective adsorption and gas detection, which was consistent with the results of the gas-sensing studies.[36,37] Enhancing gas-sensing performance is a complex process that not only depends on the specific surface area of the material but also involves the collective effect of various factors. For instance, the activity of adsorption sites is an important factor that cannot be overlooked. The number and type of these active sites directly affect the performance of the material's gas-sensing properties. We discovered that even among materials with similar specific surface areas, the gas-sensing performance may differ due to variations in the adsorption site activity. Therefore, we need to further analyze the mechanism behind the enhancement of gas-sensing performance through other characterization methods.

The UV−vis spectra of the pure SnO_2 and $Bi_{0.02}$-$Sn_{0.98}O_2$ are shown in Figure 6. All samples exhibited strong ultraviolet absorption peaks. The band gap is a crucial parameter for semiconductor materials, and SnO_2 is a typical direct semiconductor material. In this study, the Tauc method was used to calculate the band gap energy (E_g): $(\alpha h\nu)^2 = B(h\nu - E_g)$, where α is the absorption coefficient, h is the Plank constant, ν is the photon frequency, and B is a constant relative to the material.[38] The inset shows plots of $(\alpha h\nu)^2$ versus $h\nu$ for pure SnO_2 and $Bi_{0.02}$-$Sn_{0.98}O_2$. The linear portions of the

https://doi.org/10.1021/acsomega.3c09632
ACS Omega 2024, 9, 27932−27944

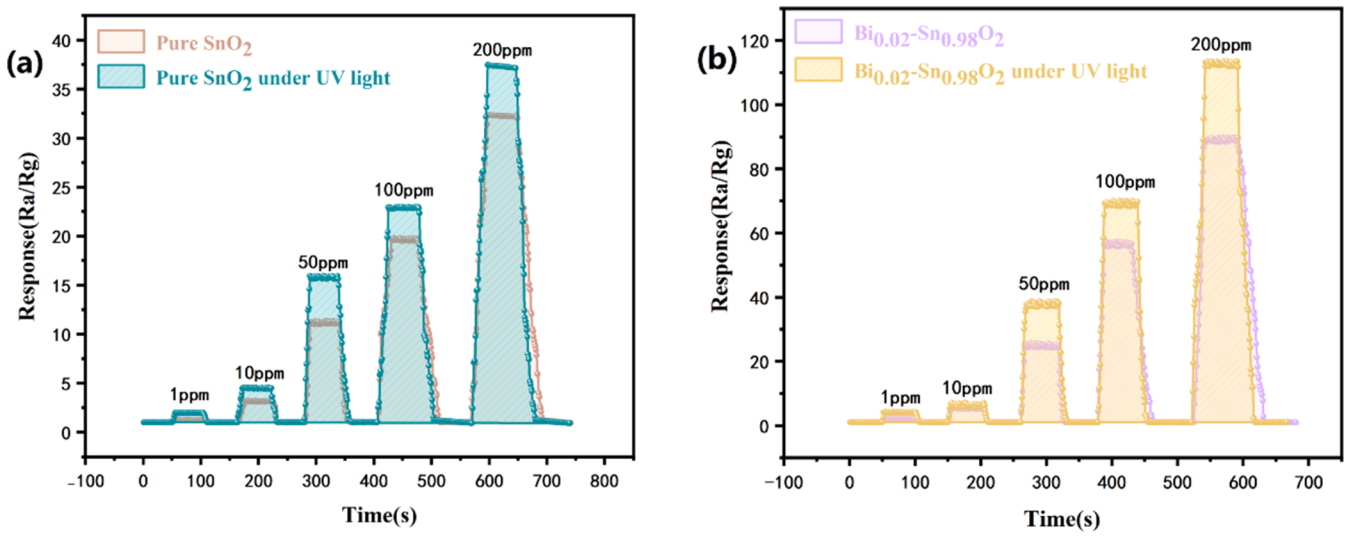

Figure 9. (a, b) Response−recovery curves for pure SnO_2 and $Bi_{0.02}$-$Sn_{0.98}O_2$ with 1−200 ppm butanone.

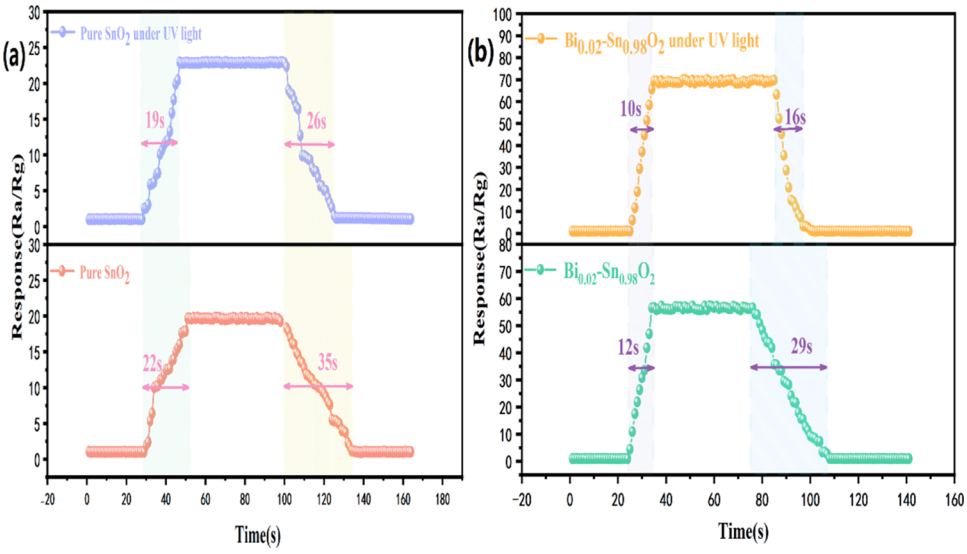

Figure 10. (a, b) Response−recovery curves for detection of 100 ppm butanone by the pure SnO_2 and $Bi_{0.02}$-$Sn_{0.98}O_2$ sensors at the optimal working temperature.

curves were extended to the horizontal axis (y = 0), and the intercept is the band gap. The calculated band gaps were 3.51 and 3.30 eV for pure SnO_2 and $Bi_{0.02}$-$Sn_{0.98}O_2$, respectively. The introduction of Bi_2O_3 resulted in a decrease in the band gap, which was attributed to an increase in the number of surface defects and a synergistic effect from the heterojunctions between the SnO_2 and Bi_2O_3 particles.[36] A lower band gap energy facilitates electron transfer from the valence band to the conduction band, resulting in enhanced gas sensitivity.[5] In the gas sensitivity tests, we employed UV light with a wavelength of 365 nm to irradiate the samples. The photon energy was calculated with the formula $E_g = 1240/\lambda$ and yielded a value of 3.40 eV, which exceeded the band gap of the material after loading. This facilitated the absorption of photons that promoted electrons from the valence band to the conduction band, and more electron−hole pairs were produced. This enhancement of the carrier density contributed to the heightened gas sensitivity of the material.[39]

To analyze the elemental composition and chemical states of the material surface, X-ray photoelectron spectroscopy (XPS) was applied to pure SnO_2 and $Bi_{0.02}$-$Sn_{0.98}O_2$. All spectra were calibrated with the C 1s peak at 284.8 eV, as shown in Figure 7. Figure 7a contains the full XPS spectrum from $Bi_{0.02}$-$Sn_{0.98}O_2$, in which the peaks for Sn, O, and Bi can be observed. This indicated the presence of Sn, O, and Bi in the material. Figure 7b−d contains the high-resolution Bi 4f, Sn 3d, and O 1s spectra, respectively. The high-resolution Bi 4f spectrum is contained in Figure 7b. The peak at approximately 164 eV was attributed to the Bi $4f_{5/2}$ state, while the peak at approximately 159 eV corresponded to the Bi $4f_{7/2}$ state. This indicated the presence of Bi^{3+} on the surface of the material.[40,41] The high-resolution Sn 3d spectrum is shown in Figure 7c. The binding energies of the two peaks were approximately 486.8 and 495.2 eV for the Sn $3d_{5/2}$ and Sn $3d_{3/2}$ states, respectively, and the distance between the two peaks was 8.4 eV. This indicated the presence of Sn^{4+} in the sample, which was consistent with results reported in the literature.[22,42] The high-resolution O 1s spectrum is illustrated in Figure 7d. As shown, three types of oxygen species were present on the surface of the material. The peak at approximately 529.5 eV was associated with the lattice

https://doi.org/10.1021/acsomega.3c09632
ACS Omega 2024, 9, 27932−27944

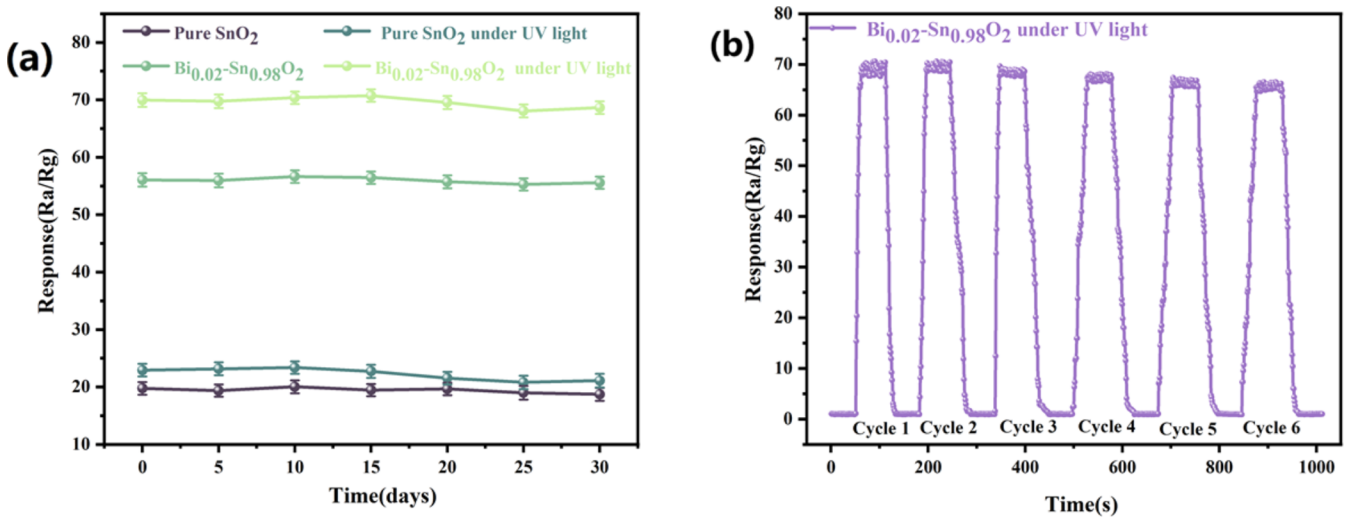

Figure 11. (a) Stability curves for pure SnO_2 and $Bi_{0.02}$-$Sn_{0.98}O_2$ exposed to 100 ppm butanone and (b) response curves of $Bi_{0.02}$-$Sn_{0.98}O_2$ after six cycles of testing.

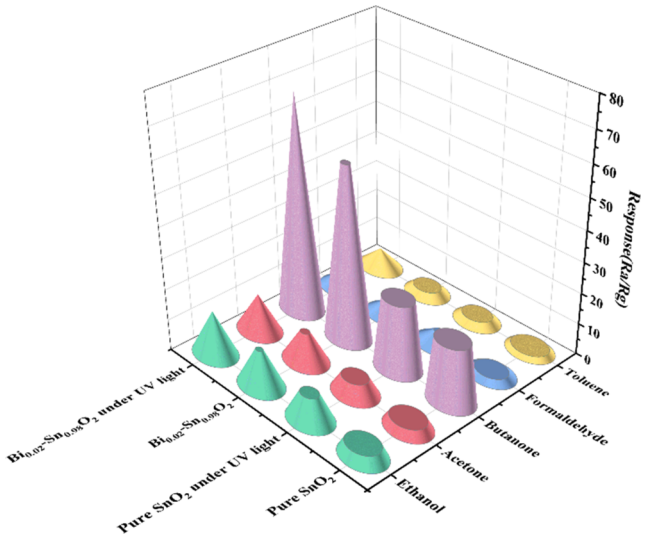

Figure 12. Responses of the pure SnO_2 and $Bi_{0.02}$-$Sn_{0.98}O_2$ sensors to 100 ppm concentrations of different VOCs at the optimal operating temperature.

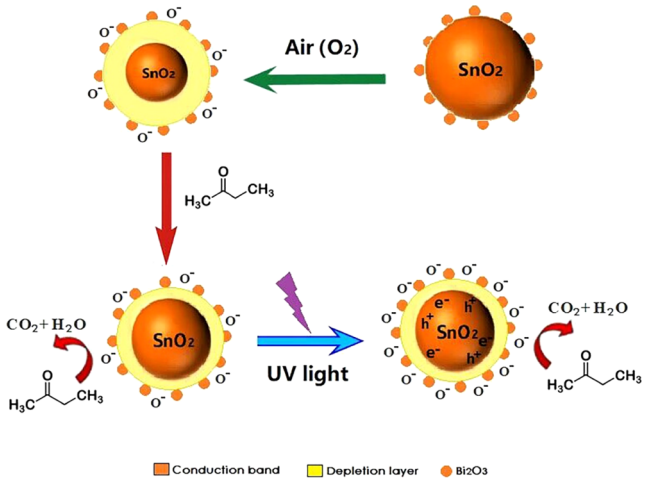

Figure 13. Schematic illustration of the mechanism for the synergistic effect of UV light irradiation and Bi_2O_3 loading in enhancing the ability of SnO_2 to detect butanone.

Table 1. Performance Comparison of Butanone Gas Sensors Reported in the Literature with the $Bi_{0.02}$-$Sn_{0.98}O_2$ Butanone Gas Sensors

materials	Con. (ppm)	response (s)	T (°C)	refs
Pt/ZnO	100	35.2	450	6
SiO_2@CoO	100	44.7	350	7
Cr_2O_3/WO_3	100	40.5	180	46
LaCoO/ZnO	100	25.0	320	47
Fe_2O_3	100	25.8	170	48
$ZnCo_2O_4$/ZnO	100	80.0	300	49
$Bi_{0.02}$-$Sn_{0.98}O_2$	100	70.2	225	this work

oxygen (O_L) present on the surface of the material, while that at approximately 531.2 eV was linked to oxygen defects (O_V) on the surface. Additionally, the peak at approximately 532.5 eV corresponded to chemically adsorbed oxygen (O_C) on the surface of the material.[43,44] In comparison with those of pure SnO_2, the O_V and O_C concentrations in the $Bi_{0.02}$-$Sn_{0.98}O_2$ sample were significantly higher. The abundant O_V sites provided more sites for adsorption and reactions of gases on the surface of the sensing material. The increased O_C proportion suggested that more oxygen species were adsorbed on the material surface.[1,18] It was inferred that samples loaded with Bi_2O_3 had superior gas sensitivities.

Gas-Sensing Performance. Generally, the sensitivity of a gas-sensitive material to the target gas is strongly correlated with the working temperature. Therefore, we examined the relationship between the operating temperature and the capabilities of samples with different Bi_2O_3 loading ratios to detect 100 ppm of butanone (with or without UV illumination). The results are depicted in Figure 8. In the temperature range of 75−225 °C, the gas sensitivities of all samples increased gradually with increases in the working temperature, irrespective of whether they were exposed to ultraviolet light. As the working temperature increased further, the responses of the gas sensors to butanone gradually decreased for all samples. According to literature reports, as the working temperature is increased, the amount of oxygen adsorbed on the surface gradually increases, leading to faster

https://doi.org/10.1021/acsomega.3c09632
ACS Omega 2024, 9, 27932−27944

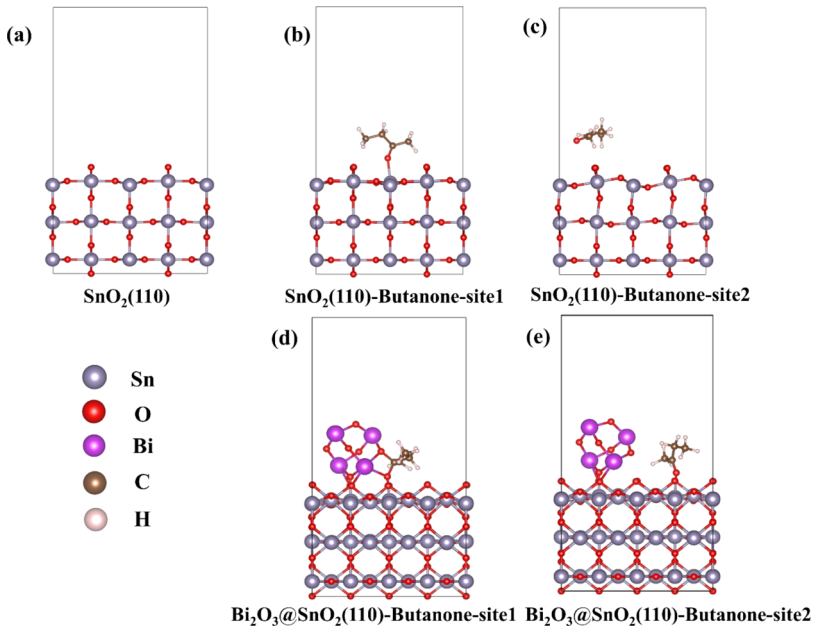

Figure 14. (a) Optimized model for SnO_2 (110). (b–e) Models for adsorption of butanone at different sites.

Table 2. Adsorption Energy of Butanone Adsorption at Different Adsorption Sites on the Unloaded and Bi-Loaded SnO_2(110) Surface

system	E_{ab} (eV)
SnO_2–C_4H_8O-site1	−0.98592172
SnO_2–C_4H_8O-site2	−0.84687376
SnO_2–Bi_2O_3–C_4H_8O-site1	−1.35208063
SnO_2–Bi_2O_3–C_4H_8O-site2	−1.04281025

reactions between the target gas and the material surface. When the temperature exceeded the optimum operating temperature, the oxygen species on the surface of the material were desorbed, resulting in a decrease in the response.[1,18] In addition, we observed an interesting phenomenon. During irradiation with 365 nm UV light, the optimal working temperatures of the $Bi_{0.02}$-$Sn_{0.98}O_2$ and $Bi_{0.03}$-$Sn_{0.97}O_2$ samples decreased. This was attributed to the generation of photogenerated electron–hole pairs when the surface of the material was irradiated with UV light. The reactions between the holes and the adsorbed oxygen species increased the electron concentration within the material, which improved the gas sensitivity of the material.[25] After a comprehensive analysis, we concluded that 225 °C was the optimal working temperature. With the optimal working temperature, the $Bi_{0.02}$-$Sn_{0.98}O_2$ samples exhibited the highest responses in the dark or when exposed to UV radiation. Therefore, we selected pure SnO_2 and $Bi_{0.02}$-$Sn_{0.98}O_2$ for the subsequent gas sensitivity study.

To evaluate the sensitivities of the two samples to various butanone concentrations, we carried out dynamic response–recovery tests. Figure 9a,b shows the dynamic response–recovery curves for detection of 1–200 ppm butanone by the two sensors at their optimal operating temperature. It is evident that as the butanone gas concentration was increased, both sensor responses also increased. As the concentration in the system rose, the growth of the response values gradually decelerated. This was most likely attributable to saturation of the active sites on the surface of the material. Meanwhile, our findings indicated that the responses of the Bi containing sensors were superior to that of pure SnO_2. After exposure to UV light, the sensor showed a significant enhancement in its ability to detect butanone at different concentration levels. Furthermore, when the gas concentration dropped to 1 ppm, even the sensor based on pure SnO_2 still provided a response of approximately 1.3 without UV light. This suggested that our synthetic sensing material had the capacity to detect low concentrations of butanone, with a detection limit of approximately 1 ppm.

The response–recovery time is a crucial parameter used in evaluating the rates for adsorption and desorption of the targeted gas from a sensor. The quicker the response and recovery times are, the more exceptional the performance of the sensor. This indicates the importance of real-time monitoring. The response–recovery curves for detection of 100 ppm butanone by the pure SnO_2 or $Bi_{0.02}$-$Sn_{0.98}O_2$ at the optimal operating temperature and with or without UV light are depicted in Figure 10a,b. Without exposure to UV light, the response time of the pure SnO_2 sensor was 22 s, and the recovery time was 35 s. The $Bi_{0.02}$-$Sn_{0.98}O_2$-based sensor exhibited a faster response time of 12 s and a shorter recovery time of 29 s. When exposed to UV light, the SnO_2-based sensor exhibited a response time of 19 s and a recovery time of 26 s, and the $Bi_{0.02}$-$Sn_{0.98}O_2$ sensor had a response time of 10 s and a recovery time of 16. After thorough examination of the collected data, it was clear that the introduction of Bi_2O_3 into the surface of the material or exposing it to UV light resulted in substantial improvements in both the response and recovery times.

Stability refers to the capacity of a sensor material to resist external interference for a specified time. It is also an important parameter used to evaluate the capabilities of sensors in practical applications. We investigated the responses of the sensors containing pure SnO_2 and $Bi_{0.02}$-$Sn_{0.98}O_2$ to 100 ppm butanone at the optimal working temperature for over a month, as shown in Figure 11a. As shown in the graph, there was a gradual reduction in the sensor response as time progressed. This indicated that the sensitive material exhibited satisfactory stability. The reduced response was likely due to

https://doi.org/10.1021/acsomega.3c09632
ACS Omega 2024, 9, 27932–27944

environmental factors such as the temperature.[45] The reversibility is another important parameter that reflects the sensor performance. We tested the sensors based on the $Bi_{0.02}$-$Sn_{0.98}O_2$ for six consecutive cycles of 100 ppm butanone at 225 °C, and the results are shown in Figure 11b. From the figure, it can be seen that after six testing cycles, the sensors had small fluctuations and could still maintain a high response.

Selectivity refers to the ability of a gas sensor to identify a specific gas within a mixture, and it is a crucial metric for evaluating the anti-interference performance. Figure 12 shows the selectivities of the samples based on pure SnO_2 and $Bi_{0.02}$-$Sn_{0.98}O_2$ in response to various VOCs at the optimal working temperature. We compared the responses of the two sensors when they were exposed to ethanol, acetone, butanone, formaldehyde, and toluene with or without UV light exposure. The graph shows that after the addition of Bi_2O_3 or exposure to UV light, the responses of the material to all VOCs were improved to varying extents. Despite this, it still exhibited a high response to butanone, indicating that the synthesized material had excellent selectivity.

Table 1 summarizes the gas sensitivities of the $Bi_{0.02}$-$Sn_{0.98}O_2$ three-dimensional hierarchical structure and those of previously reported butanone gas sensors. From the table, it is evident that the sensor utilizing $Bi_{0.02}$-$Sn_{0.98}O_2$ exhibited better responses than most sensors. Therefore, we conclude that the sensor based on $Bi_{0.02}$-$Sn_{0.98}O_2$ has enormous potential for real-time butanone detection.

Gas-Sensing Mechanism. The gas-sensing mechanisms of n-type semiconductor materials (such as SnO_2) can be described with the spatial charge model.[44,50] When SnO_2-based sensors are exposed to air, oxygen is adsorbed on the surface. The adsorbed oxygen captures electrons from the SnO_2 conduction band and forms negatively charged oxygen ions on the material surface (O_2^-, O^-, O^{2-}). As this progresses, the concentration of electrons in the SnO_2 conduction band gradually decreases, leading to the formation of a wider electron depletion layer on the material surface. This increases the resistance of the material. In our previous studies, we reported a close relationship between the types of oxygen anions and the temperature of the surrounding environment.[1] This can be shown as follows

$$O_2(\text{gas}) \rightarrow O_2(\text{ads}) \quad (1)$$

$$O_2(\text{ads}) + e^- \rightarrow O_2^-(\text{ads}) (T < 100\ ^\circ\text{C}) \quad (2)$$

$$O_2^-(\text{ads}) + e^- \rightarrow 2O^-(\text{ads}) (100\ ^\circ\text{C} < T < 300\ ^\circ\text{C}) \quad (3)$$

$$O^-(\text{ads}) + e^- \rightarrow O^{2-}(\text{ads}) (T > 300\ ^\circ\text{C}) \quad (4)$$

When reducing gases, such as butanone, are introduced into the system, they react with the adsorbed oxygen anions and release electrons back into the conduction band of the material. This reduces the thickness of the electron depletion layer and decreases the resistance of the material. The reaction is as follows[51]

$$CH_3COCH_2CH_3 + 11O^- \leftrightharpoons 4H_2O + 4CO_2 + 11e^- \quad (5)$$

Compared to the pure SnO_2 sensor, the Bi_2O_3-loaded SnO_2 sensors exhibited significantly enhanced detection of butanone. Based on the literature, SnO_2 is a representative n-type semiconductor material with a band gap energy of 3.6 eV and a work function of 4.9 eV. On the other hand, Bi_2O_3 is also a typical n-type semiconductor with a band gap energy of 2.8 eV and a work function of 5.04 eV.[52,53] Due to the lower work function of SnO_2 compared to Bi_2O_3, when these nanoparticles come into contact, the electrons serving as carriers migrate from SnO_2 to Bi_2O_3, resulting in a wider depletion layer on the SnO_2 surface. The resistance of the SnO_2 sensor loaded with Bi_2O_3 in air is significantly higher than the resistance of a pure SnO_2 sensor in air. When a Bi_2O_3-loaded SnO_2 sensor is placed in a butanone atmosphere, more oxygen adsorbed on the material surface reacts with the butanone, releasing more electrons back into the conduction band and resulting in an enhanced sensitivity and stability of the sensor.[54]

It was observed that gas sensing was significantly improved when the sensor was irradiated with UV light. According to literature reports, the surface of the material generates a substantial quantity of photogenerated electrons and holes under UV irradiation. The concentrations of O^- species on the surface of sensing materials tend to increase. This process can be described as follows[55]

$$O_2^- + e_{h\nu}^- \rightarrow 2O^- \quad (6)$$

Additionally, the oxygen vacancy defects on the surface of the material also facilitate the formation of O^- species. With this synergistic effect, the concentrations of O^- species on the surface of the material are greatly increased, thus providing more active sites. When reducing gases are introduced into the system, many O^- species participate in the oxidation reactions occurring on the surface, thereby enhancing the gas-sensing response. Moreover, exposure to UV light diminishes the activation energy of the surface oxidation reactions, resulting in reduced response−recovery times.[56]

Based on the above discussion, the synergistic mechanism for the effects of UV irradiation and Bi_2O_3 loading on the ability of SnO_2 to detect butanone is shown in Figure 13.

First-principles calculations based on density functional theory have been widely used in determining the electronic structures of semiconductor materials.[57] In our study, we developed surface atomic models for SnO_2 with and without Bi_2O_3, as well as a model for butanone adsorption at various sites. These models were evaluated with first-principles calculations, ensuring accuracy and reliability of the simulations. The density functional theory computations were carried out with CASTEP and the ultrasoft pseudopotential.[58,59] The exchange−correlation potential was determined with the Perdew−Burke−Ernzerhof (PBE) functional within the generalized gradient approximation (GGA).[60] The cutoff energy for the plane-wave-basis expansion was set to 450 eV, and the convergence factors for the energy, force, and maximum displacement were 1.0×10^{-5} eV/atom, 3.0×10^{-2} eV/Å and 1.0×10^{-3} Å, respectively. The *k*-point grid sampling of the Monkhorst−Pack scheme was set as $2 \times 2 \times 1$ in the irreducible Brillouin zone. The vacuum layer width was 15 Å. Meanwhile, the DFT-D correction method was used to describe the long-range van der Waals interactions.[61] As is widely known, the (110) surface of SnO_2 exhibited the highest thermal stability. Therefore, this paper was focused on the (110) surface of SnO_2 for research purposes. The optimized model is illustrated in Figure 14.

The optimized model for SnO_2(110) is illustrated in Figure 14a. We calculated the butanone adsorption energy for the samples with and without Bi_2O_3 loading. There were three sites for butanone adsorption on the surface of the material, Sn 5c (as shown in Figure 14b,e), O 2c (as shown in Figure 14c),

https://doi.org/10.1021/acsomega.3c09632
ACS Omega 2024, 9, 27932−27944

and Bi_2O_3 (as shown in Figure 14d). The energy (E_{ab}) of butanone adsorption was defined as

$$E_{ab} = E(\text{sub} + \text{butanone}) - E(\text{sub}) - E(\text{butanone}) \quad (7)$$

where E(sub + N_2) and E(sub) are the total energies of the system with and without butanone, respectively. E(butanone) is the total energy of butanone. Table 2 presents the energies (E_{ab}) for butanone adsorption at different adsorption sites on the unloaded and Bi-loaded SnO_2(110) surface. The table shows that the adsorption energies for different sites on the pure SnO_2(110) surface were −0.99 and −0.85 eV. With Bi_2O_3 loading, the adsorption energies at the different sites were −1.35 and −1.04 eV, respectively. The greater the adsorption energy is, the stronger the bonding between the gas and the material surface.[12,62] Therefore, it can be inferred that when Bi_2O_3 was loaded on the surface of the SnO_2 material, the system showed enhanced adsorption of butanone. This effectively enhanced the ability of the material to detect butanone, which was consistent with our experimental results.

CONCLUSIONS

We have successfully synthesized Bi_2O_3-loaded SnO_2 with a three-dimensional hierarchical structure using a combination of facile hydrothermal and impregnation precipitation methods. The gas-sensing tests conducted with butanone revealed exceptional performance under UV illumination, characterized by remarkable responses and response−recovery times (at 225 °C, the loaded sample achieved a response of 70, while the respective response−recovery times were 10 and 16 s). Moreover, our comprehensive physicochemical analyses revealed the key role of the unique hierarchical structure in facilitating efficient gas distribution. With the addition of Bi_2O_3, the surface of the sample showed a notable increase in reactive oxygen species (O^-) following UV irradiation. Theoretical calculations have further elucidated the mechanism behind this enhancement, revealing that the introduction of Bi_2O_3 significantly enhances the material surface adsorption capacity for butanone, thus augmenting its gas-sensing performance. In summary, our findings underscore the pivotal role of Bi_2O_3 loading and UV exposure in enhancing the sensing capabilities of SnO_2, offering promising avenues for advanced gas-sensing applications.

AUTHOR INFORMATION

Corresponding Author

Shantang Liu − *Key Laboratory for Green Chemical Process of Ministry of Education, School of Chemistry and Environmental Engineering, Wuhan Institute of Technology, Wuhan 430074, P. R. China*; orcid.org/0000-0002-6403-8388; Email: stliu@wit.edu.cn

Authors

Wenjie Bi − *School of Chemistry and Pharmaceutical Engineering, Hefei Normal University, Hefei 230601, P. R. China*

Hu Chen − *School of Chemistry and Pharmaceutical Engineering, Hefei Normal University, Hefei 230601, P. R. China*

Shiwei Yang − *School of Chemistry and Pharmaceutical Engineering, Hefei Normal University, Hefei 230601, P. R. China*

Xiaohong Wang − *School of Chemistry and Pharmaceutical Engineering, Hefei Normal University, Hefei 230601, P. R. China*

Aoying Liu − *School of Chemistry and Pharmaceutical Engineering, Hefei Normal University, Hefei 230601, P. R. China*

Xinyue Ma − *School of Chemistry and Pharmaceutical Engineering, Hefei Normal University, Hefei 230601, P. R. China*

Haijiao Xie − *Hangzhou Yanqu Information Technology Co., Ltd., Hangzhou 310003, P. R. China*

Complete contact information is available at: https://pubs.acs.org/10.1021/acsomega.3c09632

Notes

The authors declare no competing financial interest.

ACKNOWLEDGMENTS

This work is financially supported by the Key Projects of Natural Science Research in Universities of Anhui Province (No. KJ2021A0921), the National Natural Science Foundation of China (No. 21471120), the Science and Technology Major Project of Anhui Province of China (201903a07020003), the Hefei Normal University 2022 Scientific Research Launch Fund for Introducing High level Talents (2022rcjj26, 2022rcjj35, 2022rcjj42), the Science and Technology Major Project of Fuyang of Anhui Province of China (FK20208018), the Anhui Engineering Laboratory Project for the Development and Utilization of Natural Resources Derived from Medicines and Edibles (YSTY2022020), and the Hefei Normal University School-level Scientific Research Natural Science Key Project (2021KJZD11). The authors would like to thank H.X. from Shiyanjia Lab (www.shiyanjia.com) and Hangzhou Yanqu Information Technology Co., Ltd for purchasing the license of Materials Studio.

REFERENCES

(1) Bi, W.; Wang, W.; Liu, S. Synthesis of Rh−SnO_2 nanosheets and ultra-high triethylamine sensing performance. *J. Alloys Compd.* **2020**, *817*, No. 152730, DOI: 10.1016/j.jallcom.2019.152730.

(2) He, K.; Jin, Z.; Chu, X.; Bi, W.; Wang, W.; Wang, C.; Liu, S. Fast response−recovery time toward acetone by a sensor prepared with Pd doped WO_3 nanosheets. *RSC Adv.* **2019**, *9* (49), 28439−28450.

(3) Jiang, W.; Wei, D.; Zhang, S.; Chuai, X.; Sun, P.; Liu, F.; Xu, Y.; Gao, Y.; Liang, X.; Lu, G. The facile synthesis of MoO_3microsheets and their excellent gas-sensing performance toward triethylamine: high selectivity, excellent stability and superior repeatability. *New J. Chem.* **2018**, *42* (18), 15111−15120.

(4) Xu, K.; Yang, L.; Zou, J.; Yang, Y.; Li, Q.; Qu, Y.; Ye, J.; Yuan, C. Fabrication of novel flower-like Co_3O_4 structures assembled by single-crystalline porous nanosheets for enhanced xylene sensing properties. *J. Alloys Compd.* **2017**, *706*, 116−125.

(5) Liu, X.; Qin, X.; Ji, H.; Wang, M. An enhanced butanone sensing performance of $Er_{0.7}Yb_{0.3}FeO_3$ material with the proper electronic structure. *J. Alloys Compd.* **2019**, *772*, 263−271.

(6) Oliveira, T. N. T.; Zito, C. A.; Perfecto, T. M.; Azevedo, G. M.; Volanti, D. P. ZnO twin-rods decorated with Pt nanoparticles for butanone detection. *New J. Chem.* **2020**, *44* (36), 15574−15583.

(7) Vioto, G. C. N.; Perfecto, T. M.; Zito, C. A.; Volanti, D. P. Enhancement of 2-butanone sensing properties of SiO_2@CoO core-shell structures. *Ceram. Int.* **2020**, *46* (14), 22692−22698.

(8) Weng, Y.; Zhang, L.; Zhu, W.; Lv, Y. One-step facile synthesis of coral-like Zn-doped SnO_2 and its cataluminescence sensing of 2-butanone. *J. Mater. Chem. A* **2015**, *3* (13), 7132−7138.

(9) Zhang, Q.; Zhang, H.; Xu, M.; Shen, Z.; Wei, Q. A WO_3 nanorod-Cr_2O_3 nanoparticle composite for selective gas sensing of 2-butanone. *Chin. Chem. Lett.* **2018**, *29* (3), 538−542.
(10) Li, Y.; Luo, N.; Sun, G.; Zhang, B.; Jin, H.; Lin, L.; Bala, H.; Cao, J.; Zhang, Z.; Wang, Y. Synthesis of porous nanosheets-assembled ZnO/$ZnCo_2O_4$ hierarchical structure for TEA detection. *Sens. Actuators, B* **2019**, *287*, 199−208.
(11) Xiao, L.; Shu, S.; Liu, S. A facile synthesis of Pd-doped SnO_2 hollow microcubes with enhanced sensing performance. *Sens. Actuators, B* **2015**, *221*, 120−126.
(12) Li, N.; Fan, Y.; Shi, Y.; Xiang, Q.; Wang, X.; Xu, J. A low temperature formaldehyde gas sensor based on hierarchical SnO/SnO_2 nano-flowers assembled from ultrathin nanosheets: Synthesis, sensing performance and mechanism. *Sens. Actuators, B* **2019**, *294*, 106−115.
(13) Meng, D.; Liu, D.; Wang, G.; Shen, Y.; San, X.; Li, M.; Meng, F. Low-temperature formaldehyde gas sensors based on NiO-SnO_2 heterojunction microflowers assembled by thin porous nanosheets. *Sens. Actuators, B* **2018**, *273*, 418−428.
(14) Wang, C.; Du, G.; Ståhl, K.; Huang, H.; Zhong, Y.; Jiang, J. Z. Ultrathin SnO_2 Nanosheets: Oriented Attachment Mechanism, Nonstoichiometric Defects, and Enhanced Lithium-Ion Battery Performances. *J. Phys. Chem. C* **2012**, *116* (6), 4000−4011.
(15) Xiao, L.; Xu, S.; Yu, G.; Liu, S. Efficient hierarchical mixed Pd/SnO_2 porous architecture deposited microheater for low power ethanol gas sensor. *Sens. Actuators, B* **2018**, *255*, 2002−2010.
(16) Yang, J.; Li, X.; Wu, J.; Han, Y.; Wang, Z.; Zhang, X.; Xu, Y. Yolk-shell (Cu,Zn)Fe_2O_4 ferrite nano-microspheres with highly selective triethylamine gas-sensing properties. *Dalton Trans.* **2020**, *49* (41), 14475−14482.
(17) Dong, S.; Wu, D.; Gao, W.; Hao, H.; Liu, G.; Yan, S. Multi-dimensional templated synthesis of hierarchical Fe_2O_3/NiO composites and their superior ethanol sensing properties promoted by nanoscale p-n heterojunctions. *Dalton Trans.* **2020**, *49* (4), 1300−1310.
(18) Bi, W.; Xiao, W.; Liu, S. Synthesis of Pt-doped SnO_2 flower-like hierarchical structure and its gas sensing properties to isopropanol. *J. Mater. Sci.* **2021**, *56* (10), 6095−6109.
(19) Li, Y. X.; Guo, Z.; Su, Y.; Jin, X. B.; Tang, X. H.; Huang, J. R.; Huang, X. J.; Li, M. Q.; Liu, J. H. Hierarchical Morphology-Dependent Gas-Sensing Performances of Three-Dimensional SnO_2 Nanostructures. *ACS Sens.* **2017**, *2* (1), 102−110.
(20) Zhu, K.; Ma, S.; Tie, Y.; Zhang, Q.; Wang, W.; Pei, S.; Xu, X. Highly sensitive formaldehyde gas sensors based on Y-doped SnO_2 hierarchical flower-shaped nanostructures. *J. Alloys Compd.* **2019**, *792*, 938−944.
(21) Qin, H.; Liu, T.; Liu, J.; Liu, Q.; Li, R.; Zhang, H.; Wang, J. Fabrication of uniform 1-D ZnO/$ZnCo_2O_4$ nano-composite and enhanced properties in gas sensing detection. *Mater. Chem. Phys.* **2019**, *228*, 66−74.
(22) Yan, Y.; Liu, J.; Zhang, H.; Song, D.; Li, J.; Yang, P.; Zhang, M.; Wang, J. One-pot synthesis of cubic $ZnSnO_3$/ZnO heterostructure composite and enhanced gas-sensing performance. *J. Alloys Compd.* **2019**, *780*, 193−201.
(23) David, S. P. S.; Veeralakshmi, S.; Sandhya, J.; Nehru, S.; Kalaiselvam, S. Room temperature operatable high sensitive toluene gas sensor using chemiresistive Ag/Bi_2O_3 nanocomposite. *Sens. Actuators, B* **2020**, *320*, No. 128410, DOI: 10.1016/j.snb.2020.128410.
(24) Postica, V.; Gröttrup, J.; Adelung, R.; Lupan, O.; Mishra, A. K.; de Leeuw, N. H.; Ababii, N.; Carreira, J. F. C.; Rodrigues, J.; Sedrine, N. B.; Correia, M. R.; Monteiro, T.; Sontea, V.; Mishra, Y. K. Multifunctional Materials: A Case Study of the Effects of Metal Doping on ZnO Tetrapods with Bismuth and Tin Oxides. *Adv. Funct. Mater.* **2017**, *27* (6), No. 1604676, DOI: 10.1002/adfm.201604676.
(25) Espid, E.; Taghipour, F. Development of highly sensitive ZnO/In_2O_3 composite gas sensor activated by UV-LED. *Sens. Actuators, B* **2017**, *241*, 828−839.
(26) Kumar, R.; Liu, X.; Zhang, J.; Kumar, M. Room-Temperature Gas Sensors Under Photoactivation: From Metal Oxides to 2D Materials. *Nanomicro Lett.* **2020**, *12* (1), No. 164, DOI: 10.1007/s40820-020-00503-4.
(27) Zhang, Z.; Gao, Z.; Fang, R.; Li, H.; He, W.; Du, C. UV-assisted room temperature NO_2 sensor using monolayer graphene decorated with SnO_2 nanoparticles. *Ceram. Int.* **2020**, *46* (2), 2255−2260.
(28) Hyodo, T.; Urata, K.; Kamada, K.; Ueda, T.; Shimizu, Y. Semiconductor-type SnO_2-based NO_2 sensors operated at room temperature under UV-light irradiation. *Sens. Actuators, B* **2017**, *253*, 630−640.
(29) Saidi, T.; Palmowski, D.; Babicz-Kiewlicz, S.; Welearegay, T. G.; El Bari, N.; Ionescu, R.; Smulko, J.; Bouchikhi, B. Exhaled breath gas sensing using pristine and functionalized WO_3 nanowire sensors enhanced by UV-light irradiation. *Sens. Actuators, B* **2018**, *273*, 1719−1729.
(30) Bi, W.; Liu, S. Preparation of a hierarchical 3D structure composed of Co-doped SnO_2 nanosheets with excellent gas sensitivity to acetic acid. *Mater. Sci. Eng., B* **2022**, *286*, No. 116006.
(31) Bouras, K.; Rehspringer, J. L.; Schmerber, G.; Rinnert, H.; Colis, S.; Ferblantier, G.; Balestrieri, M.; Ihiawakrim, D.; Dinia, A.; Slaoui, A. Optical and structural properties of Nd doped SnO_2 powder fabricated by the sol−gel method. *J. Mater. Chem. C* **2014**, *2* (39), 8235−8243.
(32) Qiao, L.; Bing, Y.; Wang, Y.; Yu, S.; Liang, Z.; Zeng, Y. Enhanced toluene sensing performances of Pd- loaded SnO_2 cubic nanocages with porous nanoparticle-assembled shells. *Sens. Actuators, B* **2017**, *241*, 1121−1129.
(33) Cho, Y. H.; Liang, X.; Kang, Y. C.; Lee, J.-H. Ultrasensitive detection of trimethylamine using Rh-doped SnO_2 hollow spheres prepared by ultrasonic spray pyrolysis. *Sens. Actuators, B* **2015**, *207*, 330−337.
(34) Xing, X.; Xiao, X.; Wang, L.; Wang, Y. Highly sensitive formaldehyde gas sensor based on hierarchically porous Ag-loaded ZnO heterojunction nanocomposites. *Sens. Actuators, B* **2017**, *247*, 797−806.
(35) Chen, H. D.; Jin, K. L.; Xu, J. C.; Han, Y. B.; Jin, H. X.; Jin, D. F.; Peng, X. L.; Hong, B.; Li, J.; Yang, Y. T.; Gong, J.; Ge, H. L.; Wang, X. Q. High-valence cations-doped mesoporous nickel oxides nanowires: Nanocasting synthesis, microstructures and improved gas-sensing performance. *Sens. Actuators, B* **2019**, *296*, No. 126622, DOI: 10.1016/j.snb.2019.126622.
(36) Shu, S.; Wang, M.; Yang, W.; Liu, S. Synthesis of surface layered hierarchical octahedral-like structured Zn_2SnO_4/SnO_2 with excellent sensing properties toward HCHO. *Sens. Actuators, B* **2017**, *243*, 1171−1180.
(37) Zhang, W.; Cheng, X.; Zhang, X.; Xu, Y.; Gao, S.; Zhao, H.; Huo, L. High selectivity to ppb-level HCHO sensor based on mesoporous tubular SnO_2 at low temperature. *Sens. Actuators, B* **2017**, *247*, 664−672.
(38) Gao, F.; Li, Y.; Zhao, Y.; Wan, W.; Du, G.; Ren, X.; Zhao, H. Facile synthesis of flower-like hierarchical architecture of SnO_2 nanoarrays. *J. Alloys Compd.* **2017**, *703*, 354−360.
(39) Tian, J.; Chen, X.; Wang, T.; Pei, W.; Li, F.; Li, D.; Yang, Y.; Dong, X. Modification of indium oxide nanofibers by polyoxometalate electron acceptor doping for enhancement of gas sensing at room temperature. *Sens. Actuators, B* **2021**, *344*, No. 130227, DOI: 10.1016/j.snb.2021.130227.
(40) Gao, C.; Liu, G.; Liu, X.; Wang, X.; Liu, M.; Chen, Y.; Jiang, X.; Wang, G.; Teng, Z.; Yang, W. Flower-like n-Bi_2O_3/n-BiOCl heterojunction with excellent photocatalytic performance for visible light degradation of Bisphenol A and Methylene blue. *J. Alloys Compd.* **2022**, *929*, No. 167296, DOI: 10.1016/j.jallcom.2022.167296.
(41) Reddy, N. L.; Emin, S.; Valant, M.; Shankar, M. V. Nanostructured Bi_2O_3@TiO_2 photocatalyst for enhanced hydrogen production. *Int. J. Hydrogen Energy* **2017**, *42* (10), 6627−6636, DOI: 10.1016/j.ijhydene.2016.12.154.

https://doi.org/10.1021/acsomega.3c09632
ACS Omega 2024, 9, 27932−27944

(42) Shao, S.; Chen, X.; Chen, Y.; Lai, M.; Che, L. Ultrasensitive and highly selective detection of acetone based on Au@WO_3-SnO_2 corrugated nanofibers. *Appl. Surf. Sci.* **2019**, *473*, 902−911.
(43) Chen, G.; Chu, X.; Qiao, H.; Ye, M.; Chen, J.; Gao, C.; Guo, C.-Y. Thickness controllable single-crystal WO_3 nanosheets: Highly selective sensor for triethylamine detection at room temperature. *Mater. Lett.* **2018**, *226*, 59−62.
(44) Kou, X.; Xie, N.; Chen, F.; Wang, T.; Guo, L.; Wang, C.; Wang, Q.; Ma, J.; Sun, Y.; Zhang, H.; Lu, G. Superior acetone gas sensor based on electrospun SnO_2 nanofibers by Rh doping. *Sens. Actuators, B* **2018**, *256*, 861−869.
(45) Yu, Q.; Zhang, Y.; Xu, Y. Hierarchical hollow $BiFeO_3$ microcubes with enhanced acetone gas sensing performance. *Dalton Trans.* **2021**, *50* (19), 6702−6709.
(46) Zhang, Q.; Xu, M.; Shen, Z.; Wei, Q. A nanostructured Cr_2O_3/WO_3 p−n junction sensor for highly sensitive detection of butanone. *J. Mater. Sci.: Mater. Electron.* **2017**, *28* (16), 12056−12062.
(47) Qin, W.; Yuan, Z.; Gao, H.; Zhang, R.; Meng, F. Perovskite-structured $LaCoO_3$ modified ZnO gas sensor and investigation on its gas sensing mechanism by first principle. *Sens. Actuators, B* **2021**, *341*, No. 130015, DOI: 10.1016/J.SNB.2021.130015.
(48) Liu, W.-X.; Sun, J.-B.; Li, Y.-N.; Kong, D.-R.; Song, B.-Y.; Zhang, X.-F.; Deng, Z.-P.; Xu, Y.-M.; Huo, L.-H.; Gao, S. Low-temperature and high-selectivity butanone sensor based on porous Fe_2O_3 nanosheets synthesized by phoenix tree leaf template. *Sens. Actuators, B* **2023**, *377*, No. 133054, DOI: 10.1016/j.snb.2022.133054.
(49) Zhu, H.; Ji, H.; Zhang, R.; Mu, Z.; Liu, Y.; Yuan, Z.; Shen, Y.; Meng, F. Ppb-level butanone sensor based on porous spherical $ZnCo_2O_4$/ZnO through the synergy effects of Co^{2+} atoms and unique wrinkled structure. *Sens. Actuators, B* **2023**, *393*, No. 134087, DOI: 10.1016/j.snb.2023.134087.
(50) Kou, X.; Wang, C.; Ding, M.; Feng, C.; Li, X.; Ma, J.; Zhang, H.; Sun, Y.; Lu, G. Synthesis of Co-doped SnO_2 nanofibers and their enhanced gas-sensing properties. *Sens. Actuators, B* **2016**, *236*, 425−432.
(51) Zhu, H.; Qin, W.; Li, J.; Yuan, Z.; Meng, F.; Shen, Y. Investigation on Butanone Sensing Properties of ZnO Sensor Under Different Calcination Temperature. *IEEE Sens. J.* **2022**, *22* (1), 25−32.
(52) Fan, H.; Li, H.; Liu, B.; Lu, Y.; Xie, T.; Wang, D. Photoinduced charge transfer properties and photocatalytic activity in Bi_2O_3/$BaTiO_3$ composite photocatalyst. *ACS Appl. Mater. Interfaces* **2012**, *4* (9), 4853−4857.
(53) Chu, L.; Zhang, J.; Wu, Z.; Wang, C.; Sun, Y.; Dong, S.; Sun, J. Solar-driven photocatalytic removal of organic pollutants over direct Z-scheme coral-branch shape Bi_2O_3/SnO_2 composites. *Mater. Charact.* **2020**, *159*, No. 110036, DOI: 10.1016/j.matchar.2019.110036.
(54) Yang, T.; Gu, K.; Zhu, M.; Lu, Q.; Zhai, C.; Zhao, Q.; Yang, X.; Zhang, M. ZnO-SnO_2 heterojunction nanobelts: Synthesis and ultraviolet light irradiation to improve the triethylamine sensing properties. *Sens. Actuators, B* **2019**, *279*, 410−417.
(55) Wang, J.; Shen, Y.; Li, X.; Xia, Y.; Yang, C. Synergistic effects of UV activation and surface oxygen vacancies on the room-temperature NO_2 gas sensing performance of ZnO nanowires. *Sens. Actuators, B* **2019**, *298*, No. 126858, DOI: 10.1016/j.snb.2019.126858.
(56) Nikfarjam, A.; Salehifar, N. Improvement in gas-sensing properties of TiO_2 nanofiber sensor by UV irradiation. *Sens. Actuators, B* **2015**, *211*, 146−156.
(57) Li, M.; Zhu, H.; Wei, G.; He, A.; Liu, Y. DFT calculation and analysis of the gas sensing mechanism of methoxy propanol on Ag decorated SnO_2 (110) surface. *RSC Adv.* **2019**, *9* (61), 35862−35871.
(58) Kresse, G.; Joubert, D. From ultrasoft pseudopotentials to the projector augmented-wave method. *Phys. Rev. B* **1999**, *59* (3), No. 1758, DOI: 10.1103/PhysRevB.59.1758.
(59) Kresse, G.; Furthmüller, J. Efficiency of ab-initio total energy calculations for metals and semiconductors using a plane-wave basis set. *Comput. Mater. Sci.* **1996**, *6* (1), 15−50.
(60) Perdew, J. P.; Burke, K.; Ernzerhof, M. Generalized gradient approximation made simple. *Phys. Rev. Lett.* **1996**, *77* (18), 3865.
(61) Grimme, S.; Antony, J.; Ehrlich, S.; Krieg, H. A consistent and accurate ab initio parametrization of density functional dispersion correction (DFT-D) for the 94 elements H-Pu. *J. Chem. Phys.* **2010**, *132* (15), No. 154104.
(62) Xue, D.; Wang, P.; Zhang, Z.; Wang, Y. Enhanced methane sensing property of flower-like SnO_2 doped by Pt nanoparticles: A combined experimental and first-principle study. *Sens. Actuators, B* **2019**, *296*, No. 126710, DOI: 10.1016/j.snb.2019.126710.

https://doi.org/10.1021/acsomega.3c09632
ACS Omega 2024, 9, 27932−27944